Zinc and Cadmium Complexation of L-Threonine: An Infrared Multiple Photon Dissociation Spectroscopy and Theoretical Study

Georgia C. Boles,[†] Randy L. Hightower,[†] Giel Berden,[‡] Jos Oomens,[‡,#] and P. B. Armentrout[*,†]*

[†]Department of Chemistry, University of Utah, 315 S. 1400 E. Rm. 2020, Salt Lake City, Utah 84112, United States

[‡]Radboud University, Institute for Molecules and Materials, FELIX Laboratory, Toernooiveld 7, NL-6525 ED Nijmegen, The Netherlands

[#]van'‍t Hoff Institute for Molecular Sciences, University of Amsterdam, Science Park 904, NL-1098 XH Amsterdam, The Netherlands

* Corresponding author, e-mail: armentrout@chem.utah.edu

Abstract: Complexes of threonine (Thr) cationized with Zn^{2+} and Cd^{2+} were examined by infrared multiple photon dissociation action spectroscopy using light generated from a free electron laser. Low-energy conformers for $Zn(Thr\text{-}H)^+(ACN)$ (where ACN = acetonitrile), $Zn(Gly\text{-}H)^+(ACN)$ (formed via CO_2-laser irradiation of intact $Zn(Thr\text{-}H)^+(ACN)$), and $CdCl^+(Thr)$ complexes were found using quantum chemical calculations in order to identify the structures formed experimentally. For all species, the predicted ground structures reproduce the experimental spectra well, where tridentate [N,CO,OH_s] binding motifs were dominantly observed for the intact $Zn(Thr\text{-}H)^+(ACN)$ and $CdCl^+(Thr)$ complexes. In both of these cases, the metal center binds to the backbone amino group (N), carbonyl oxygen (CO, where this site is deprotonated in the Zn^{2+} complex), and side-chain hydroxyl oxygen (OH_s). For the Zn^{2+} system, there also appears to be a population of a higher-energy species in which the side chain is deprotonated, either [N,O_s^-,CO] or [N,O_s^-,OH]. CO_2-laser irradiation of $Zn(Thr\text{-}H)^+(ACN)$ leads to loss of its side chain via elimination of acetaldehyde, yielding a bidentate $Zn(Gly\text{-}H)^+[N,CO^-](ACN)$ complex. Overall, this work explores the binding interactions between Thr and biologically relevant metals in a prototypical environment. Comparison of current work with previous analyses allows for the

elucidation of important metal dependent trends associated with physiologically important metal–amino acid binding.

INTRODUCTION

In the first step of protein translation, aminoacyl-tRNA synthetases (AARS) enzymatically catalyze the aminoacylation reaction via covalently linking an amino acid to its corresponding tRNA.[1-4] Thus, the accurate translation of genetic code is highly dependent on the ability of AARS to distinguish between amino acids characterized by similar composition, a function that becomes increasingly difficult when isosteric residues or those with similar side-chain chemistry compete for binding. The amino acid recognition of the zinc ion (Zn^{2+}) present in threonyl-tRNA synthetase (ThrRS) has been previously evaluated, where the ability of ThrRS to discriminate against isosteric valine (Val) and structurally similar serine (Ser) is important.[5] High selectivity of Thr was observed, where specifically, it was determined that ThrRS activates Ser at a rate that is 1,000-fold lower than that of Thr, whereas Val showed no competitive activation.[5] Given the similar side-chain chemistry of Thr and Ser, a pairwise analysis of prototypical Zn^{2+}–Thr/Ser binding (as well as the investigation of the metal–induced changes observed upon Zn^{2+} replacement with its cadmium congener, Cd^{2+}) could elucidate important fundamental information regarding the factors that govern metal binding to each of these amino acids. Furthermore, this work also lays the foundation for further studies that could evaluate the analogous binding in larger, more biologically relevant systems.

In the present work, conformations of the experimentally formed $Zn(Thr–H)^+(ACN)$, $Zn(Gly–H)^+(ACN)$ (formed via CO_2-laser irradiation of the intact $Zn(Thr–H)^+(ACN)$ complex), and $CdCl^+(Thr)$ complexes were determined via IRMPD action spectroscopy. In each case, comparison of the calculated and experimental spectra allows for clear identification of the occupied conformation(s). Action spectra for each complex were measured and compared to theoretical spectra calculated at the B3LYP/6-311+G(d,p) (Zn^{2+} complexes) or B3LYP/def2-TZVP (Cd^{2+} complexes) levels of theory, where an SDD effective core potential was used for

cadmium. These combinations of levels of theory and basis sets have been used previously in the successful evaluations of Zn^{2+} and Cd^{2+} cationized histidine (His),[6] cysteine (Cys) and cysteine methyl ester (Cys-OMe),[7] glutamine (Gln),[8] serine (Ser),[9] asparagine (Asn),[10] glutamic acid (Glu),[11] aspartic acid (Asp),[12] arginine (Arg),[13] and lysine (Lys).[14]

EXPERIMENTAL AND COMPUTATIONAL SECTION

Mass Spectrometry and Photodissociation. Experiments were performed at the free electron lasers for infrared experiments (FELIX) facility at Radboud University in the Netherlands.[15] A 4.7 T Fourier transform ion cyclotron resonance (FT-ICR) mass spectrometer, described elsewhere,[16-18] was used to measure the IRMPD spectra. Ions were generated using an electrospray ionization (ESI) source and then accumulated in a hexapole trap for about 4 s before being pulse extracted through a quadrupole bender and injected into the ICR cell via a radiofrequency (rf) octopole ion guide. Electrostatic switching of the dc bias of the octopole was used to trap the ions in the ICR cell without collisional heating of the ions.[17] Once trapped in the ICR cell, the ion of interest (assumed to be roughly at room temperature) was mass selected using a stored waveform inverse Fourier transform (SWIFT) excitation pulse.[19-20] These ions were irradiated with FELIX for 0.5 – 3 s at a 10 Hz macropulse repetition rate (energy up to 60 mJ per pulse and a bandwidth of 0.5% of the central frequency). The IRMPD spectra for the Zn^{2+} complexes were generated by plotting the photofragmentation yield, defined here as $Y = -\ln(\Sigma I_P / (\Sigma I_P + \Sigma I_F))$,[21] where I_P and I_F are the integrated intensities of the precursor and fragment ion mass peaks (where the sum includes all isotopes), respectively, as a function of the frequency of IR radiation. In all cases, yield was linearly corrected for frequency dependent variation in the laser power, which may result in yields slightly above unity. Linear corrections result in higher relative intensities of the high frequency bands and minor changes in the low frequency region. The application of a linear laser power correction is well described in the literature[21-22] and is appropriate because the power dependence is basically linear until saturation

begins because of the incoherent rather than coherent nature of the multiple photon excitation process.

Metallated Thr complexes were prepared from solutions of 1.0 mM Thr and 1.0 mM $Zn(NO_3)_2$ or $CdCl_2$ in 60:40 MeOH/H_2O solvent using a Micromass Z-Spray ESI source. Flow rates of 6 μL/min were used, and the electrospray needle was held at a voltage of 3.0 kV. In the case of Zn^{2+}, the ESI source generated $Zn(Thr\text{-}H)^+(ACN)$, in which Thr is deprotonated and an acetonitrile (ACN, CH_3CN) ligand is also bound. (The ACN was present adventitiously from previous experiments.) A continuous wave CO_2 laser (30 W) was used to irradiate $Zn(Thr\text{-}H)^+(ACN)$ for 0.1 s in an attempt to remove the ACN ligand, although this instead yielded $Zn(Gly\text{-}H)^+(ACN)$ in which the ACN remained bound to the Zn^{2+} metal center and $(Thr\text{-}H)^-$ lost its acetaldehyde side chain. The resulting ions were mass isolated and allowed to cool radiatively for 0.4 s.[23] Electrospray ionization of the Cd^{2+} solution generated $CdCl^+(Thr)$.

It should be noted that previous studies involving zinc(II) complexes of amino acids (AA) have resulted in electrospray formation of $Zn(AA\text{-}H)^+$ species, both in our previous work[6-8, 10, 12-14] as well as earlier work by Ohanessian and co-workers.[24-27] Both series of works also demonstrate that different solvent conditions may lead to differences in intensity as well as formation of different complexes. Additional factors such as the experimental setup and operating pressures may also affect the complexes formed. In the current study, the adventitious presence of ACN resulted in the preferential formation of the 4-coordinate $Zn(Thr\text{-}H)^+(ACN)$ complex (as demonstrated below) such that $Zn(Thr\text{-}H)^+$ could not be isolated despite altering the solution conditions. Tight binding between the metal center and the ACN ligand has been documented previously, e.g., in the case of $Zn(Glu\text{-}H)^+(ACN)$, the ACN remains bound even upon irradiation with FELIX.[11]

Computational Details. In order to determine low-lying conformers of the cationized Thr complexes, geometries analogous to those previously reported for $Zn(Ser–H)^+(ACN)$ and $CdCl^+(Ser)$ were used as initial starting structures.[9] For all complexes, the Gaussian 09 suite of programs was used.[28] Initial optimization of the metallated complexes was then done at the

B3LYP/6-31G(d) level of theory using the "loose" keyword to utilize a large step size of 0.01 au and an rms force constant of 0.0017 to facilitate convergence. Unique structures were then further optimized at the B3LYP/6-311+G(d,p) level of theory for Zn^{2+} complexes. For Cd^{2+} complexes, the B3LYP/def2-TZVP level, where def2-TZVP is a size-consistent basis set for all atoms and includes triple-ζ + polarization functions with a small core (28 electrons) effective core potential (ECP) on Cd, was used.[29-30] The def2-TZVP basis set and corresponding SDD ECP were obtained from the EMSL basis set exchange.[31] These combinations of level of theory, basis set, and SDD ECP have proven previously to provide accurate structural information with complexes of similar size and composition.[6-14] Geometry optimizations of low-energy metallated structures were also conducted including corrections for empirical dispersion at the B3LYP-GD3BJ level[32-33] using the same basis sets.

Vibrational frequencies were scaled by 0.975 for comparison to the IRMPD spectra, where this scaling factor has been shown to account for known inaccuracies in the calculated frequencies, and therefore gives good agreement with well-resolved peaks in other IRMPD spectra.[6-14] The calculated frequencies were broadened using a 25 cm^{-1} full-width at half maximum Gaussian line shape when used for comparison to the experimentally determined spectra. This broadening accounts for the finite laser bandwidth, unresolved rotational structure of the ions (which are near room temperature), anharmonicity of the vibrational mode, use of different isotopes in constructing the experimental spectra (see Supporting Information Table S1), and broadening as a result of the multiple photon absorption process.[34]

Relative energies were determined from B3LYP geometries using single point energies calculated at the B3LYP, B3P86, and MP2(full) levels using 6-311+G(2d,2p) (Zn^{2+} complexes) and def2-TZVPP (Cd^{2+} complexes) basis sets. Relative B3LYP-GD3BJ single point energies using these larger basis sets and the B3LYP-GD3BJ geometries were also computed for the lowest-energy species. Zero-point energy (ZPE) corrections were applied to single point energies in order to provide 0 K relative enthalpies. Thermal corrections to obtain 298 K Gibbs energies were calculated from 0 K relative enthalpies by using the rigid rotor/harmonic oscillator approximation

with the calculated rotational constants and vibrational frequencies. Vibrational frequencies were scaled by 0.989 when used for zero point energy (ZPE) and thermal corrections.[35]

RESULTS AND DISCUSSION

IRMPD Action Spectroscopy. IRMPD action spectra were measured over the 600 – 1800 cm^{-1} (16.6 – 5.6 μm) range for the $Zn(Thr\text{-}H)^+(ACN)$ and $CdCl^+(Thr)$ complexes and the 1000 – 1800 cm^{-1} (10.0 – 5.6 μm) range for the $Zn(Gly\text{-}H)^+(ACN)$ species. In each case, the main IR induced fragments (detailed below) were used to determine the yield spectrum.

Fragmentation pathways observed for the Zn^{2+} species are given in reactions 1 and 2, where the number in brackets indicates the mass-to-charge ratio (*m/z*) of the ion using ^{64}Zn (49.17% natural abundance) as the precursor ion. Channels corresponding to ^{66}Zn and ^{68}Zn (27.73 and 18.45% natural abundance, respectively) were also monitored and included in yield calculations.[36] As shown in reaction 1, IRMPD of $Zn(Thr\text{-}H)^+(ACN)$ results in the loss of acetaldehyde, yielding an ion having a mass consistent with $Zn(Gly\text{-}H)^+(ACN)$. IRMPD of the isolated putative $Zn(Gly\text{-}H)^+(ACN)$ ions formed via CO_2-laser irradiation of $Zn(Thr\text{-}H)^+(ACN)$ results in ACN dissociation, as shown in reaction 2.

$$Zn(Thr\text{-}H)^+(ACN)\,[223] + n\,h\nu \rightarrow Zn(Gly\text{-}H)^+(ACN)\,[179] + CH_3CHO \quad (1)$$

$$Zn(Gly\text{-}H)^+(ACN)\,[179] + n\,h\nu \rightarrow Zn(Gly\text{-}H)^+\,[138] + ACN \quad (2)$$

IRMPD of $CdCl^+(Thr)$ results in the fragmentation pathways given in reactions 3 and 4. Masses are chosen to correspond to the most abundant isotopes of Cd and Cl, ^{114}Cd (28.75 %) and ^{35}Cl (75.5 %),[36] such that *m/z* 268 is designated as the precursor ion. The $CdCl^+(Thr)$ complexes associated with *m/z* values corresponding to ^{113}Cd (12.23 %), ^{112}Cd (24.11 %), ^{111}Cd (12.80 %), ^{110}Cd (12.47 %), and ^{37}Cl (24.5 %) were also monitored and included in yield calculations.

$$CdCl^+(Thr)\,[268] + n\,h\nu \rightarrow CdCl^+(C_4H_7NO_2)\,[250] + H_2O \quad (3)$$

$$CdCl^+(C_4H_7NO_2)\,[250] + n\,h\nu \rightarrow C_3H_6N^+\,[56] + CO_2 + HCdCl \quad (4)$$

The primary dissociation pathways exhibited by the $Zn(Thr–H)^+(ACN)$ and $CdCl^+(Thr)$ systems are analogous to those observed in the similar $Zn(Ser–H)^+(ACN)$ and $CdCl^+(Ser)$ systems,

namely loss of an organic neutral in the Zn^{2+} systems (acetaldehyde and formaldehyde, respectively) and loss of water from the Cd^{2+} complexes.[9] The most notable difference is observed with the sequential loss of CO_2 + HCdCl from $CdCl^+(C_4H_7NO_2)$ leading to *m/z* 56 in the current $CdCl^+$(Thr) work. The analogous dissociation pathway was not observed in the $CdCl^+$(Ser) system, where only loss of H_2O and H_2O + CO was detected.[9]

Nomenclature. The structures of the complexes are designated by their metal binding site (N = amino nitrogen, CO = carbonyl oxygen of carboxylic acid, OH = hydroxyl oxygen of carboxylic acid, O_s = side-chain oxygen) in square brackets, with the deprotonation site (if present) indicated by a negative sign. When binding takes place at the amino site, the nitrogen is always listed first, and the additional available binding sites are ranked such that the site with the shorter metal-binding site interaction is listed next. Binding designation is followed by the amino acid orientation, which is represented by characterization of dihedral angles as *c* (cis, for angles between 0° – 45°), *g* (gauche, 45° – 135°), or *t* (trans, 135° – 180°). In a few cases, signs of the gauche angles (+ or –) are also needed in order to distinguish otherwise identical names. Dihedral angles are measured starting from the backbone carboxylic acid hydrogen (unless this site is deprotonated) or the analogous proton on NH_3^+ in zwitterionic structures, and end at the side-chain hydroxyl hydrogen (if present).

Zn(Thr-H)$^+$(ACN) Relative Energies. Relative 0 K and 298 K single point energies of located Zn(Thr-H)$^+$(ACN) complexes are given in Table 1. Two low-lying tridentate species were found (Table 1 and Figure 1) and differ in their deprotonation sites. At 298 K, B3P86 predicts that [N,O_s^-,CO]-tgg(ACN) is lowest in energy, whereas all remaining levels of theory suggest that [N,CO^-,OH_s]-ggt(ACN) is the ground structure (GS). B3P86 predicts that the GS binds zinc to the amino nitrogen, deprotonated side-chain oxygen, and carbonyl oxygen of the carboxylic acid. The B3LYP, B3LYP-GD3BJ, and MP2 predict that the GS instead deprotonates at the carboxylic acid, but binds Zn at the same three atoms. Both species bind at the nitrogen of the ACN group equivalently, as detailed below. At all levels of theory, these species are determined to be within 4 kJ/mol of each other, thus both are likely to be present experimentally. Indeed, an equilibrium

population analysis at 298 K suggests that the [N,O_s^-,CO]-tgg(ACN)/[N,CO^-,OH_s]-ggt(ACN) species should have populations of 37/63, 31/69, 58/42, and 19/81% at the B3LYP, B3LYP-GD3BJ, B3P86, and MP2 levels of theory.

No additional low-lying Zn(Thr-H)$^+$(ACN) species were located, as all higher-lying conformers located are characterized by 298 K relative energies at least 14 kJ/mol above the GS. Of these additional conformers, tridentate [N,O_s^-,CO](ACN) (Figure 1), [N,O_s^-,OH](ACN), [N^-,CO,OH_s](ACN), [N^-,OH_s,OH](ACN), and [CO_2^-,OH_s](ACN) types were located (Figure S1). All potential bidentate complexes explored were significantly higher in energy than the GSs (> 27 kJ/mol) suggesting that these species are not likely to be formed experimentally. Notably, [N,O_s^-]-tg_t(ACN) was the lowest in energy among those explored (Figure S1), lying 27 – 40 kJ/mol higher in energy than the GS at each respective level of theory.

Comparison of Experimental and Theoretical IR Spectra: Zn(Thr-H)$^+$(ACN). The experimental Zn(Thr-H)$^+$(ACN) spectrum (Figure 2) has major spectral features located at 1757, 1577, 1237, 1157, 1048, and 1014 cm^{-1}. An overview of the vibrational frequencies calculated for the five lowest energy Zn(Thr-H)$^+$(ACN) species is given in Supporting Information Table S1. The experimental spectrum is largely reproduced by the tridentate [N,CO^-,OH_s]-ggt(ACN) species, calculated to be the GS at the B3LYP, B3LYP-GD3BJ, and MP2 levels. Specifically, the [N,CO^-,OH_s]-ggt(ACN) species predicts bands at 1753 (uncoordinated CO stretch), 1601 (amino NH_2 bend), 1238 (carboxylate OCO bend, amino NH_2 rock, and CH motions), 1205 (side chain COH bend and CH motions), and 1050 cm^{-1} (amino NH_2 wag). As is typical for the amino NH_2 bend,[6-14] there is a significant shift (24 cm^{-1}) between the calculated and experimental positions. It also reproduces a number of minor bands observed experimentally between 660 – 1000 cm^{-1} and 1300 – 1550 cm^{-1}. Notably, this species does not explain the bands located at 1157 and 1014 cm^{-1} in the experimental spectrum (although it does have weak bands predicted at 1136 as well as 1022 and 997 cm^{-1}). One possible explanation for these bands would be contributions from the low-energy [N,O_s^-,CO]-tgg(ACN) species (the B3P86 GS), which exhibits calculated bands at 1181 (primarily backbone COH bend with minor contribution from amino NH_2 rock) and 1162

(primarily amino NH_2 rock with minor contribution from backbone COH bend), as well as 1009 cm^{-1} (amino NH_2 wag). However, this species has additional intense bands predicted at 1423 (backbone COH bend and CH motions) and 1663 cm^{-1} (coordinated CO stretch, COH bend, and amino NH_2 bend). There is no experimental evidence for such strong bands, although weak peaks are observed at these frequencies. Thus, this species cannot be the dominant species formed experimentally. This is consistent with B3LYP, B3LYP-GD3BJ, and MP2 levels of theory, which suggest that [N,CO^-,OH_s]-ggt(ACN) is the GS with a 298 K population of [N,O_s^-,CO]-tgg(ACN) of only 19 – 37% (see above).

Also shown in Figure 2 is the spectral comparison between the experimental Zn(Thr-H)$^+$(ACN) spectrum and calculated spectrum for the next highest energy conformer, [N,O_s^-,CO]-cgg(ACN), which also fails to reproduce most of the intense experimental spectral features and has intense spectral features not seen experimentally. The same is true for the lowest energy species deprotonated at the nitrogen, [N^-,CO,OH_s]-tggt(ACN), as shown in Figure S2. Additional bidentate species were explored and none better reproduce the spectrum. Specifically, comparisons between the experimental spectrum and calculated spectra for [N,O_s^-]-tg_t(ACN) and [N,CO^-]-gtt(ACN) were made. Of these, [N,CO^-]-gtt(ACN) reproduces many of the experimental features reasonably well, with the exception of the two intense bands located in the 1000 – 1100 cm^{-1} region (Figure S2). Another possible explanation for the 1157 and 1014 cm^{-1} bands is the high-energy tridentate [N,O_s^-,OH]-tgg(ACN), calculated to lie 36 – 39 kJ/mol above the GS. As shown in Figure 2, this species has its two most intense bands at 1129 (COH bend coupled with CNH bend) and 1023 (NH_2 umbrella) cm^{-1}. Because the carbonyl is no longer bound to the zinc, its CO stretch lies at 1864 cm^{-1}, just outside the range of the experimental spectrum. Figure S2 shows that a sum of the [N,CO^-,OH_s]-ggt(ACN) and [N,O_s^-,OH]-tgg(ACN) reproduces the entire spectrum reasonably well; however, the population of such a high-energy species, especially one that binds to the hydroxyl group rather than to the carbonyl of the carboxylic acid group is unusual and has not been seen in any of our other examinations of zinc cationized amino acids.[6-14]

Given this uncertainty, additional more exotic species were explored. In particular, we considered the Thr ligand rearrangement mentioned above in which the acetaldehyde side chain has dissociated to deprotonated glycine and CH_3CHO, with both retained on the Zn, $Zn(Gly\text{-}H)^+(CH_3CHO)(ACN)$ (Figure S1 and Table 1). Interestingly, this species is actually lower in energy than the $Zn(Thr\text{-}H)^+(ACN)$ GS by 6 – 47 kJ/mol. (Although we did not explicitly examine the mechanism for formation of this species, its production requires activation, presumably because substantial rearrangement is involved. In particular, a hydrogen atom must move from the carboxylic acid to the central carbon of the acetaldehyde.) Its IR spectrum is also shown in Figure 2, where it can be seen that the acetaldehyde group has a CO stretch at 1671 cm^{-1}, for which there is no experimental evidence. We also checked a $Zn(Gly)^+(CH_3CO)(ACN)$ species (Figure S1), a plausible intermediate on the pathway to forming the acetaldehyde leaving group. Here, the CO stretch of the glycine is located at 1694 cm^{-1} and the CO stretch of the CH_3CO ligand mixes with the NH_2 scissors motion to form two bands at 1631 and 1646 cm^{-1}. Again this is inconsistent with the experimental spectrum in this region. At the suggestion of a referee, we also considered structures in which a covalent ZnH moiety was formed. Of several possibilities tried, formation of the ZnH bond always led to dissociation of the (Thr-2H) ligand, resulting in either $ZnH(C_3H_7ON)^+(CO_2)(ACN)$ or $ZnH(Gly\text{-}2H)^+(CH_3CHO)(ACN)$, as shown in Figure S1 (with energies given in Table 1). Both species are high in energy (>50 kJ/mol above the GS) and neither have an IR spectrum that reproduces the experiment (e.g., a single band at 1683 cm^{-1} and a triplet at 1667, 1701, and 1722 cm^{-1}, respectively).

Therefore, it is determined that a dominant contribution from the B3LYP, B3LYP-GD3BJ, and MP2 predicted $[N,CO^-,OH_s]$-ggt(ACN) GS reproduces the spectrum. A minor contribution from the B3P86 predicted GS, $[N,O_s^-,CO]$-tgg(ACN), could explain two additional intense bands observed experimentally, but its presence is contraindicated by the failure to observe two other intense bands predicted for this species. Contributions from a $[N,O_s^-,OH]$-tgg(ACN) conformer are consistent with the observed spectrum, but the formation of such a high energy species has no precedent in our previous studies of related molecules.

Zn(Thr-H)$^+$(ACN) Structural Analysis. An overview of key geometric parameters calculated for all located Zn(Thr-H)$^+$(ACN) species is given in Table S2 of the Supporting Information. General trends observed follow those found previously in similar systems.[6 – 14] Specifically, sites of deprotonation characteristically lead to shorter Zn–X bond lengths. Deprotonation of the backbone CO leads to Zn–O distances of 1.86 – 1.90 Å, whereas the intact [N,CO] type structures have Zn–O lengths at least 0.2 Å longer, ranging from 2.10 to 2.19 Å Likewise, conformers exhibiting N$^-$ deprotonation sites are characterized by Zn–N bond lengths ranging from 1.81 – 1.88 Å, whereas species in which this site is intact have Zn–N bond lengths at least 0.15 Å longer. The largest difference is observed at the side-chain hydroxyl oxygen site. [N,O$_s^-$] type structures have Zn–O$_s$ bond lengths of 1.82 – 1.89 Å, whereas intact [N,OH$_s$] conformers exhibit Zn–O$_s$ bond lengths ranging from 2.14 – 2.30 Å.

Here, a more detailed analysis of the predicted GSs is presented. For the lowest energy [N,CO$^-$,OH$_s$]-ggt(ACN) and [N,O$_s^-$,CO]-tgg(ACN) species, bond distances between comparable sites are generally similar. In particular, the distance between the zinc and the deprotonation site in each complex is comparable (1.90 Å in[N,CO$^-$,OH$_s$]-ggt(ACN) and 1.86 Å in the [N,O$_s^-$,CO]-tgg(ACN) complex). Likewise, the difference in bond lengths between zinc and the secondary oxygen binding site is 0.05 Å, where [N,CO$^-$,OH$_s$]-ggt(ACN) exhibits the shorter distance, 2.14 Å. Instead, the largest difference arises from Zn–N binding, where the B3P86 predicted GS, [N,O$_s^-$,CO]-tgg(ACN), exhibits a longer Zn–N bond (2.16 Å) than [N,CO$^-$,OH$_s$]-ggt(ACN), which is characterized by a 0.07 Å shorter Zn–N bond.

As discussed above, the ACN-free counterparts were not isolated experimentally. Nonetheless, these structures were theoretically explored, with selected structures shown in Figures 1 and S3. The general energetic and structural trends exhibited by the Zn(Thr-H)$^+$(ACN) species are paralleled in the ACN-free Zn(Thr-H)$^+$ complexes as detailed in Supporting Information Tables S3 and S4.

Zn(Gly-H)$^+$(ACN) Relative Energies. As given in Table 2 and Figure 3, several low-energy Zn(Gly-H)$^+$(ACN) conformers were located theoretically. At all levels of theory,

deprotonation at the carboxylic acid is lowest in energy, where $Zn(Gly\text{-}H)^+[N,CO^-]$-c(ACN) (Figure 3) lies at least 6 kJ/mol lower in energy at 298 K than all additional located species. Specifically, $Zn(Gly\text{-}H)^+[N,CO^-]$-c(ACN) lies 6 – 11 kJ/mol lower in energy than $Zn(Gly\text{-}H)^+[N^-,CO]$-tt(ACN), the lowest energy species located where deprotonation occurs at the amino nitrogen (Figure 3). Other species exhibiting analogous deprotonation are $Zn(Gly\text{-}H)^+[N^-,CO]$-ct(ACN) (20 – 29 kJ/mol above the GS) and $Zn(Gly\text{-}H)^+[N^-,OH]$-tc(ACN) (62 – 68 kJ/mol above the GS). Other coordination motifs include $[CO_2^-]$, $[N,CO](C_\alpha^-)$, and $[C_\alpha^-,CO]$. In the latter two, deprotonation occurs at C_α and either involves coordination at the amino nitrogen and carbonyl oxygen (tt and ct variants of $Zn(Gly\text{-}H)^+[N,CO](C_\alpha^-)$(ACN), 47 – 65 kJ/mol above the GS) or C_α and carbonyl oxygen (cc and tc variants of $Zn(Gly\text{-}H)^+[C_\alpha^-,CO]$(ACN), 85 – 104 kJ/mol above the GS). Two $[CO_2^-]$ species were located, where $Zn(Gly\text{-}H)^+[CO_2^-]$-c(ACN) is lower by 6 – 7 kJ/mol than $Zn(Gly\text{-}H)^+[CO_2^-]$-$c_{,NH\bullet CO}$(ACN) at all levels of theory at 298 K. At 0 K, the c variant is lower than $c_{,NH\bullet CO}$ at the B3LYP and B3P86 levels of theory by ~1 kJ/mol, whereas the inclusion of the NH•CO hydrogen bond in $Zn(Gly\text{-}H)^+[CO_2^-]$-$c_{,NH\bullet CO}$(ACN) alters these relationships at the MP2 level of theory such that $c_{,NH\bullet CO}$ is lower in energy than the c species, although by only 0.2 kJ/mol.

Comparison of Experimental and Theoretical IR Spectra: $Zn(Gly–H)^+$(ACN). As noted above, irradiation of $Zn(Thr\text{-}H)^+$(ACN) (either by FELIX or the CO_2 laser) leads to loss of the CH_3CHO side chain and an ion having the mass of $Zn(Gly\text{-}H)^+$(ACN). This structural assignment can be tested by the IRMPD spectrum obtained for this species. Indeed, the experimental $Zn(Gly\text{-}H)^+$(ACN) spectrum (Figure 4), with major spectral features located at 1776, 1200, and 1081 cm^{-1}, is well-reproduced by the $Zn(Gly\text{-}H)^+[N,CO^-]$-c(ACN) GS species. Here, this structure is characterized by computed bands at 1772 (uncoordinated CO stretch), 1213 (NH_2 wag and CCO bend), and 1102 cm^{-1} (NH_2 wag). All three bands are blue shifted slightly compared to experiment, suggesting a slightly different scaling factor might be better. No additional conformers better reproduce these two bands. In particular, comparison between the experimental spectrum and the calculated spectra for $Zn(Gly\text{-}H)^+[N^-,CO]$-tt(ACN) and $Zn(Gly\text{-}H)^+[CO_2^-]$-

c(ACN) are also given in Figure 4. Notably, both of these species fail to reproduce the intense band at 1776 cm^{-1} such that these conformers are not likely to be appreciably formed experimentally. This conclusion is consistent with theoretical results that suggests that $Zn(Gly\text{-}H)^+[N,CO^-]$-c(ACN) is the dominant species formed. Across all levels of theory, this structure is predicted to be > 92% populated.

$Zn(Gly\text{-}H)^+$(ACN) Structural Analysis. An overview of key geometric parameters of the located $Zn(Gly\text{-}H)^+$(ACN) species is given in Table S5. The two lowest energy species exhibit similar bond distances between the zinc metal center and site of deprotonation (1.85 and 1.83 Å for $[N,CO^-]$-c(ACN) and $[N^-,CO]$-tt(ACN), respectively). Likewise, the distances between the second coordinating site as well as the nitrogen of the ACN ligand are found to be within 0.04 Å of each other. Similar parameters are calculated for the higher energy species characterized by $[N^-,CO]$, $[N,CO](C_\alpha^-)$, and $[N^-,OH]$ coordination motifs. Notable differences are only observed for the $[CO_2^-]$ and $[C_\alpha^-,CO]$ species, which both generally exhibit longer Zn–X (X = second oxygen of carboxylate group or C_α^-) and Zn–O bond distances. Selected species are shown in Figure S4.

Several solvated $Zn(Gly\text{-}H)^+$ systems have been evaluated previously by Ohanessian and co-workers.[27] Bond distances between zinc and the deprotonated glycine are the same within 0.03 Å and between zinc and several solvents (methanal, acetone, acetonitrile, and pyridine) are within 0.01 – 0.05 Å of each other, suggesting that these interactions are not strongly solvent dependent. Here, we calculate an identical structure for the $Zn(Gly\text{-}H)^+$(ACN) complex (very small differences attributable to the different levels of theory used). It can also be noted, however, that the Zn-solvent interaction in the $Zn(Gly\text{-}H)^+$(ACN) system does slightly lengthen the bond distances between the zinc metal center and the oxygen site of deprotonation as well as the second nitrogen coordinating site (by 0.006 and 0.045 Å, respectively) when compared to the solvent free $Zn(Gly\text{-}H)^+$ system.

$CdCl^+$(Thr) Relative Energies. Similar to the $Zn(Thr\text{-}H)^+$(ACN) system, the predicted $CdCl^+$(Thr) GS species is characterized by a tridentate binding motif (Table 3 and Figure 5). At

all levels of theory, [N,CO,OH_s]-tggt is predicted to be lowest in energy, where Cd^{2+} binds to the amino nitrogen, carbonyl oxygen, and side-chain hydroxyl oxygen. An additional cggt variant was located and lies 27 – 30 kJ/mol higher in energy. Interestingly, all additional lower-energy conformers located are characterized by bidentate coordination motifs. Specifically, [N,CO]-tg_g_+t is located 15 – 26 kJ/mol above the [N,CO,OH_s]-tggt GS. Higher-energy tgtt and tgtg variants are located 19 – 32 kJ/mol above the GS. Other bidentate motifs given in Table 3 include [CO_2^-] (14 – 63 kJ/mol), [N,OH_s] (26 – 41 kJ/mol), [CO,OH_s] (43 – 59 kJ/mol), and [N,OH] (55 – 59 kJ/mol). An additional 14 higher energy conformers are described in Table S6 of the Supporting Information. These higher-lying species include [CO^-,OH_s], [O_s^-], [CO], [O_s^-,OH], [OH_s,OH], and [O_s^-,CO] conformers, all of which lie at least 59 kJ/mol above the GS. Select structures are given in Figure S5.

Comparison of Experimental and Theoretical IR Spectra: $CdCl^+$(Thr). Major experimental features of the $CdCl^+$(Thr) spectrum are observed at 1702, 1584, 1425, 1220, 1160, and 1050 cm^{-1}, as shown in Figure 6. Also given in Figure 6 are computed spectra for the three lowest energy species: [N,CO,OH_s]-tggt, [N,CO]-tg_g_+t, and [CO_2^-]-ctgt. Of these, the GS [N,CO,OH_s]-tggt reproduces the spectrum reasonably well. Here, predicted bands at 1705 (coordinated CO stretch), 1610 (amino NH_2 bend), 1414 (backbone COH bend), 1221 (side-chain COH bend), 1177 and 1158 (backbone and side-chain COH bend along with amino NH_2 rock), and 1048 cm^{-1} (primarily amino NH_2 wag) reproduce the experimental features quite well with respect to band position and intensity. Again the predicted and experimental amino NH_2 bends are shifted (by 26 cm^{-1}), as seen for other $CdCl^+$(AA) complexes.[6-14] The bidentate [N,CO]-tg_g_+t spectrum also matches experiment reasonably well, although not as well as [N,CO,OH_s]. Specifically, bands are predicted at 1684 (coordinated CO stretch), 1592 (amino NH_2 bend), 1413 (backbone COH bend), 1251 (backbone and side-chain COH bend along with amino NH_2 rock), 1178 (backbone COH bend), 1137 (amino NH_2 wag), 1082 cm^{-1} (backbone and side-chain COH bend along with amino NH_2 rock and delocalized distortions). Here, shifting is noticeable in the high frequency range, where the predicted 1684 cm^{-1} band appears red shifted compared to the

experimental 1702 cm^{-1} band. Additionally, the experimental bands at 1220 and 1050 cm^{-1} are more poorly reproduced by this species compared to the lower energy [N,CO,OH_s]-tggt structure. Other binding motifs, such as the zwitterionic [CO_2^-] structures, also do not reproduce the major spectral features. Thus, the [N,CO,OH_s]-tggt GS is identified as the species formed experimentally. This conclusion is consistent with theoretical energies that suggest the GS is populated > 99%. Scaled vibrational frequencies (along with calculated intensities) are given in Table S7 of the Supporting Information.

Comparison of the $Zn(Thr\text{-}H)^+(ACN)$ and $CdCl^+(Thr)$ complexes shows that characteristic vibrational modes (CO stretches, NH_2 bends, etc.) do experience a shift. Previous studies indicate that smaller ionic radii (where the ionic radius of Zn^{2+}, 0.60 Å, is 0.18 Å smaller than that of Cd^{2+})[36] shift major vibrational motions to lower frequencies, e.g., as observed in the comparison of $Zn(Cys\text{-}H)^+$ and $Cd(Cys\text{-}H)^+$.[7] In the present comparison, the ACN ligand pulls electron density away from the metal center such that coordination of the Thr ligand by Zn is relaxed, which strengthens the C=O bond, resulting in a shift to higher frequencies. We reached a similar conclusion in our analysis of the analogous $Zn(Ser\text{-}H)^+(ACN)$ and $CdCl^+(Ser)$ complexes, where CO stretches were observed at 1762 and 1704 cm^{-1}, respectively.[9] Intense CO stretches in the current work are similarly observed at 1757 and 1702 cm^{-1} in the $Zn(Thr\text{-}H)^+(ACN)$ and $CdCl^+(Thr)$ spectra, respectively. A smaller shift is observed for the band corresponding to the amino NH_2 bend, where experimental bands are observed at 1577 and 1584 cm^{-1} in the Zn^{2+} and Cd^{2+} spectra, respectively. In both of these cases, deprotonation and presence of the ACN ligand (in addition to metal cation size) plays a role in the shifting of similarly characterized bands.

$CdCl^+$(Thr) Structural Analysis. The tridentate [N,CO,OH_s]-tggt/cggt and [N,OH_s,OH]-tggt species have generally similar M–N (2.26 – 2.36 Å), M–OC (2.33 – 2.39 Å), and M–O_s (2.40 – 2.49 Å) bond lengths, see Supporting Information Table S8. Likewise, their tridentate coordination results in similar ∠NCdO (64.3 – 70.5°), ∠NCdO_s (68.3 – 72.1°), and ∠OCdO_s (76.4 – 76.9°) angles. [N,OH_s,OH]-tggt has a longer M–OH distance, 2.64 Å, than the M–OC bonds and a smaller ∠NCdO angle, 64.3°, mainly because binding at the backbone hydroxyl oxygen site is

less favorable than the preferred CO site. Bidentate [N,CO] type structures (with the exception of [N,CO]-ccgt) are characterized by very similar M-N (2.26 – 2.33 Å) bond lengths, with shorter M-O (2.27 – 2.36 Å) bond lengths. Here, [N,CO]-ccgt binds tighter at the backbone oxygen site such that a weaker interaction at the nitrogen is observed, where M–N and M–O bond lengths are 2.40 and 2.20 Å, respectively. For all of the zwitterionic [CO_2^-] structures given in Table S8, binding at each of the oxygen sites is not equivalent such that the two M–O distances range from 2.65 to 2.81 and 2.10 to 2.14 Å.

Compared to the Zn^{2+} systems, the Cd^{2+} species exhibit characteristically longer M-N, M-O, and M-O_s bond lengths, a consequence of the larger ionic radius of Cd^{2+} (0.78 Å) compared to Zn^{2+} (0.60 Å)[37] and a result of the deprotonated ligand for the zinc complexes. Additionally, larger angles involving the metal center (i.e., ∠NCdO, ∠NCdO_s, and ∠OCdO_s angles) are observed in the Zn^{2+} complexes. These angles range from 74.9 to 95.2°, 81.1 to 96.4°, and 82.9 to101.9°, respectively, in the Zn^{2+} complexes but are 10 to 25° smaller in the $CdCl^+$(Thr) species. These observations are consistent with structural descriptions of other Zn^{2+} and Cd^{2+}–amino acid complexes.[6-14] Further, we conducted a Natural Bond Order (NBO) analysis[38-39] of the charges on the metals in the ground structures, Zn(Thr-H)$^+$(ACN) [N,CO^-,OH_s]-ggt(ACN) and [N,O_s^-,CO]-tgg(ACN) and $CdCl^+$(Thr) [N,CO,OH_s]-tggt, finding nearly identical charges of 1.30, 1.29, and 1.25, respectively.

Comparison to Zn^{2+} and Cd^{2+} Binding to Ser. Threonine/serine selectivity (in spite of their similar side-chain characterization) plays an important role in various biological functions including the orientation of glycosidic linkages and the characterization of active site nucleophiles in proteasomes.[40-42] Given this selectivity, one could imagine that threonine/serine replacement may similarly affect protein structure at metal binding sites (e.g., zinc finger domains). Thus, we present below a description of Zn^{2+} and Cd^{2+} binding to these two similar amino acids.

For the Zn^{2+} structures, both experimentally formed Zn(Xxx-H)$^+$(ACN) species were consistent with the presence of multiple low-energy conformers. In the previously studied Zn(Ser-H)$^+$(ACN) system, density functional levels of theory suggested a [N,CO,O_s^-]-tgg GS

whereas MP2 instead predicted a [N,CO^-,OH_s]-ggt GS.[9] The experimental evidence confirmed the likely presence of both structures. [N,CO^-,OH_s]-ggt reproduces an intense CO stretch observed at ~1755 cm^{-1}, whereas [N,CO,O_s^-]-tgg reproduces a lower intensity band of similar character about 80 cm^{-1} lower in frequency.[9] Rather than an equal distribution of both conformers, spectral features instead suggested that the MP2 [N,CO^-,OH_s]-ggt GS is the dominant conformer formed experimentally. This is consistent with the current results that indicate that deprotonation occurs at the carboxylic acid in the complex most dominantly observed. Here, the [N,CO^-,OH_s]-ggt GS (predicted to be lowest in energy at all levels of theory except B3P86) is the dominant conformer, a conclusion more consistent with theoretical predictions compared to the Ser study.[9] (In the previous Zn(Ser-H)$^+$(ACN) study, only the MP2 level of theory predicted that the dominant conformer formed experimentally, Zn(Ser-H)$^+$(ACN) [N,CO^-,OH_s], was in fact the GS, whereas all levels except B3P86 predict that the analogous structure is the GS in the current work.) Structurally, these Zn(Ser–H)$^+$(ACN) [N,CO^-,OH_s] and Zn(Thr-H)$^+$(ACN) [N,CO^-,OH_s] species are quite similar, with Zn–N, Zn–O, and Zn–O_s bond distances within 0.02 Å.[9]

Likewise, both $CdCl^+$(Ser) and $CdCl^+$(Thr) exhibit tridentate [N,CO,OH_s] GSs. In both cases, each of the respective GSs fully reproduces the experimental spectrum with no evidence for additional conformers.[9] Similar to the Zn^{2+} systems, both $CdCl^+$(Ser) and $CdCl^+$(Thr) GSs are structurally similar, where Cd-N, Cd-O, and Cd-O_s bond distances of both complexes are calculated to be within 0.03 Å.[9] Thus, serine/threonine replacement in these small, prototypical systems does not strongly affect the structural characterization of these systems. However, minor changes were observed in the Zn^{2+} spectra (compared to more similar spectra in the case of the $CdCl^+$(Xxx) systems) such that effects of serine/threonine replacement may be metal dependent. (Specifically, the Zn(Ser-H)$^+$(ACN) spectrum exhibits a more pronounced band at ~1670 cm^{-1} attributable to the [N,O_s^-,CO]-tgg conformer compared to a very weak spectral response in the same region in the current work.) Additionally, threonine/serine selectivity in larger, more biologically relevant systems may be affected by higher-order structural considerations as well as the presence of aqueous media, an effect not included in these gas-phase studies.

CONCLUSIONS

IRMPD action spectra of complexes of $Zn(Thr\text{-}H)^+(ACN)$, $Zn(Gly\text{-}H)^+(ACN)$, and $CdCl^+(Thr)$ were measured and compared with theoretical IR spectra calculated at the B3LYP/6-311+G(d,p) (Zn^{2+} complexes) and B3LYP/def2-TZVP (Cd^{2+} complexes) levels of theory. In all cases, theoretically determined GSs reproduce the experimental IRMPD spectrum well. For the $Zn(Thr\text{-}H)^+(ACN)$ system, contributions from both $[N,CO^-,OH_s]$-ggt(ACN) (the predicted GS at all levels of theory except B3P86) and $[N,O_s^-,CO]$-tgg(ACN) (the B3P86 predicted GS) or $[N,O_s^-,OH]$-tgg(ACN) reproduce the spectrum reasonably well. Alternative isomers were explored and none better reproduce the spectrum. For the $Zn(Gly\text{-}H)^+(ACN)$ complex, the spectrum is reproduced well exclusively by the $Zn(Gly\text{-}H)^+[N,CO^-]$-c(ACN) GS, with no major contributions from higher-lying conformers needed. Excellent agreement was also observed for the $CdCl^+(Thr)$ species, where the $[N,CO,OH_s]$-tggt GS (predicted to be the lowest energy structure at all levels of theory) reproduces the entire spectrum well. No additional low-energy $CdCl^+(Thr)$ species were located such that contributions from additional conformers are unlikely.

Comparison to the previous analysis of $Zn(Ser\text{-}H)^+(ACN)$ and $CdCl^+(Ser)$ allowed for valuable information regarding differences in metal binding (with respect to structural and spectral considerations) between the serine and threonine systems. Only minor changes were observed in the $Zn(Ser\text{-}H)^+(ACN)$ and $Zn(Thr\text{-}H)^+(ACN)$ spectra with respect to the relative populations observed of the two predicted $Zn(Xxx\text{-}H)^+(ACN)$ GSs. In both systems, the $[N,CO^-,OH_s]$-ggt conformer is dominant, but analysis of the Ser system indicated higher abundance of the B3LYP, B3LYP-GD3BJ, and B3P86 predicted GS ($[N,O_s^-,CO]$-tgg) compared to the current analysis, which clearly indicates that the analogous species is not as appreciably populated. No obvious differences were observed in the Cd^{2+} congeners. Structurally, each of the Zn^{2+} and Cd^{2+} GSs were characterized by similar M-N, M-O, and M-O_s bond distances such that these small, single amino acid ligand systems appear to be unaffected by the minor differences in the Ser and Thr side chains. Comparison within the Thr complexes showed that characteristic vibrational modes shift with

respect to metal cation size and the presence of the ACN ligand. Additionally, the inherent difference in binding between Zn^{2+} and anionic $(Thr\text{-}H)^-$ versus $CdCl^+$ to neutral Thr also accounts for some of the spectral shifts observed. Continuation of this foundational work associated with the study of important metal–amino acid binding with larger, more biologically relevant systems would allow for a more detailed analysis of characteristic metal binding trends, work that is currently underway in our laboratory.

ASSOCIATED CONTENT

Supporting Information

The supporting information is available free of charge on the ACS Publication website at DOI: 10.1021/acs.jpcb.xxxxx

Tables S1 and S2 provide scaled vibrational frequencies for the five lowest-lying conformers of $Zn(Thr\text{-}H)^+(ACN)$ and key geometric parameters for the located $Zn(Thr\text{-}H)^+(ACN)$ structures, respectively. Tables S3 and S4 provide relative energies and key geometric parameters for located $Zn(Thr\text{-}H)^+$ structures, respectively. Table S5 gives key geometric parameters for the located $Zn(Gly\text{-}H)^+(ACN)$ species. Tables S6 – S8 provide relative energies for higher-lying $CdCl^+(Thr)$ structures, scaled vibrational frequencies for the five lowest-lying $CdCl^+(Thr)$ structures, and the key geometric parameters for the located $CdCl^+(Thr)$ species, respectively. Figure S1 gives structures of higher energy $Zn(Thr\text{-}H)^+(ACN)$ complexes and its isomers. Figure S2 compares the experimental $Zn(Thr\text{-}H)^+(ACN)$ spectrum with calculated spectra for $[N,CO^-]$-gtt(ACN), $[N^-,CO,OH_s]$-tggt(ACN), and the sum of $[N,CO^-,OH_s]$-ggt(ACN) and $[N,O_s^-,OH]$-tgg(ACN). Figures S3 – S5 show structures of higher energy $Zn(Thr\text{-}H)^+$, $Zn(Gly\text{-}H)^+(ACN)$, and $CdCl^+(Thr)$ complexes, respectively.

AUTHOR INFORMATION

Corresponding Author

*E-mail: armentrout@chem.utah.edu

ORCID
G. Berden: 0000-0003-1500-922X

J. Oomens: 0000-0002-2717-1278

P. B. Armentrout: 0000-0003-2953-6039

Notes

The authors declare no competing financial interest.

ACKNOWLEDGMENTS

Financial support for this work was provided by the National Science Foundation, Grants CHE-1664618 and OISE-1357887. We gratefully acknowledge the *Nederlandse Organisatie voor Wetenschappelijk Onderzoek* (NWO) for the support of the FELIX Laboratory. In addition, a grant of computer time from the Center of High Performance Computing at the University of Utah is greatly appreciated.

REFERENCES

1. Arnez, J. G.; Moras, D. Structural and Functional Considerations of the Aminoacylation Reaction. *Trends Biochem. Sci.* **1997,** *22*, 211-216.
2. Woese, C. R.; Olsen, G. J.; Ibba, M.; Söll, D. Aminoacyl-tRNA Synthetases, the Genetic Code, and the Evolutionary Process. *Microbiology and Molecular Biology Reviews* **2000,** *64*, 202-236.
3. Guo, M.; Yang, X.-L.; Schimmel, P. New Functions of Aminoacyl-tRNA Synthetases Beyond Translation. *Nat. Rev. Mol. Cell Biol.* **2010,** *11*, 668.
4. Pang, Y. L. J.; Poruri, K.; Martinis, S. A. tRNA Synthetase: tRNA Aminoacylation and Beyond. *Wiley Interdisciplinary Reviews: RNA* **2014,** *5*, 461-480.
5. Sankaranarayanan, R.; Dock-Bregeon, A.-C.; Rees, B.; Bovee, M.; Caillet, J.; Romby, P.; Francklyn, C. S.; Moras, D. Zinc Ion Mediated Amino Acid Discrimination by Threonyl-tRNA Synthetase. *Nat. Struct. Biol.* **2000,** *7*, 461-465.
6. Hofstetter, T. E.; Howder, C.; Berden, G.; Oomens, J.; Armentrout, P. B. Structural Elucidation of Biological and Toxicological Complexes: Investigation of Monomeric and Dimeric Complexes of Histidine with Multiply Charged Transition Metal (Zn and Cd) Cations using IR Action Spectroscopy. *J. Phys. Chem. B* **2011,** *115*, 12648-12661.
7. Coates, R. A.; McNary, C. P.; Boles, G. C.; Berden, G.; Oomens, J.; Armentrout, P. B. Structural Characterization of Gas-Phase Cysteine and Cysteine Methyl Ester Complexes with Zinc and Cadmium Dications by Infrared Multiple Photon Dissociation Spectroscopy. *Phys. Chem. Chem. Phys.* **2015,** *17*, 25799-25808.
8. Boles, G. C.; Coates, R. A.; Berden, G.; Oomens, J.; Armentrout, P. B. Experimental and Theoretical Investigations of Infrared Multiple Photon Dissociation Spectra of Glutamine Complexes with Zn^{2+} and Cd^{2+}. *J. Phys. Chem. B* **2015,** *119*, 11607–11617.
9. Coates, R. A.; Boles, G. C.; McNary, C. P.; Berden, G.; Oomens, J.; Armentrout, P. B. Zn^{2+} and Cd^{2+} Cationized Serine Complexes: Infrared Multiple Photon Dissociation Spectroscopy and Density Functional Theory Investigations. *Phys. Chem. Chem. Phys.* **2016,** *18*, 22434 – 22445.
10. Boles, G. C.; Coates, R. A.; Berden, G.; Oomens, J.; Armentrout, P. B. Experimental and Theoretical Investigations of Infrared Multiple Photon Dissociation Spectra of Asparagine Complexes with Zn^{2+} and Cd^{2+} and Their Deamidation Processes. *J. Phys. Chem. B* **2016,** *120*, 12486-12500.
11. Boles, G. C.; Owen, C. J.; Berden, G.; Oomens, J.; Armentrout, P. B. Experimental and Theoretical Investigations of Infrared Multiple Photon Dissociation Spectra of Glutamic Acid Complexes with Zn^{2+} and Cd^{2+}. *Phys. Chem. Chem. Phys.* **2017,** *19*, 12394 - 12406.
12. Boles, G. C.; Hightower, R. L.; Coates, R. A.; McNary, C. P.; Berden, G.; Oomens, J.; Armentrout, P. B. Experimental and Theoretical Investigations of Infrared Multiple Photon Dissociation Spectra of Aspartic Acid Complexes with Zn^{2+} and Cd^{2+}. *J. Phys. Chem. B* **2018,** *122*, 3836-3853.
13. Chalifoux, A. M.; Boles, G. C.; Berden, G.; Oomens, J.; Armentrout, P. B. Experimental and Theoretical Investigations of Infrared Multiple Photon Dissociation Spectra of Arginine Complexes with Zn^{2+} and Cd^{2+}. *Phys. Chem. Chem. Phys.* **2018,** *20*, 20712-20725.
14. Owen, C. J.; Boles, G. C.; Berden, G.; Oomens, J.; Armentrout, P. B. Experimental and Theoretical Investigations of Infrared Multiple Photon Dissociation Spectra of Lysine Complexes with Zn^{2+} and Cd^{2+}. *Eur. J. Mass Spectrom.* **2019,** *25*, 97-111.
15. Oepts, D.; van der Meer, A. F. G.; van Amersfoort, P. W. The Free-Electron-Laser User Facility FELIX. *Infrared Phys. Technol.* **1995,** *36*, 297-308.

16. Valle, J. J.; Eyler, J. R.; Oomens, J.; Moore, D. T.; van der Meer, A. F. G.; von Heldon, G.; Meijer, G.; Hendrickson, C. L.; Marshall, A. G.; Blakney, G. T. Free Electron Laser-Fourier Transform Ion Cyclotron Resonance Mass Spectrometry Facility for Obtaining Infrared Multiphoton Dissociation Spectra of Gaseous Ions. *Rev. Sci. Instrum.* **2005,** *76*, 023103.
17. Polfer, N. C.; Oomens, J.; Moore, D. T.; von Helden, G.; Meijer, G.; Dunbar, R. C. Infrared Spectroscopy of Phenylalanine Ag(I) and Zn(II) Complexes in the Gas Phase. *J. Am. Chem. Soc.* **2006,** *128*, 517-525.
18. Polfer, N. C.; Oomens, J. Reaction products in mass spectrometry elucidated with infrared spectroscopy. *Phys. Chem. Chem. Phys.* **2007,** *9*, 3804-3817.
19. Marshall, A. G.; Wang, T. C. L.; Ricca, T. L. Tailored excitation for Fourier transform ion cyclotron mass spectrometry. *J. Am. Chem. Soc.* **1985,** *107*, 7893-7897.
20. Guan, S.; Marshall, A. G. Stored Waveform Inverse Fourier Transform (SWIFT) Ion Excitation in Trapped-ion Mass Spectometry: Theory and Applications. *Int. J. Mass Spectrom. Ion Process.* **1996,** *157-158*, 5-37.
21. Berden, G.; Derksen, M.; Houthuijs, K. J.; Martens, J.; Oomens, J. An Automatic Variable Laser Attenuator for IRMPD Spectroscopy and Analysis of Power-dependence in Fragmentation Spectra. *Int. J. Mass Spectrom.* **2019,** *443*, 1-8.
22. Lemaire, J.; Boissel, P.; Heninger, M.; Mauclaire, G.; Bellec, G.; Mestdagh, H.; Le Caer, S.; Ortega, J.; Glotin, F.; Maître, P. Gas Phase Infrared Spectroscopy of Selectively Prepared Ions. *Phys. Rev. Lett.* **2002,** *89*, 273002.
23. Dunbar, R. C. Infrared Radiative Cooling of Isolated Polyatomic Molecules. *J. Chem. Phys.* **1989,** *90*, 7369-7375.
24. Rogalewicz, F.; Hoppilliard, Y.; Ohanessian, G. Structures and fragmentations of zinc(II) complexes of amino acids in the gas phase. I. Electrosprayed ions which are structurally different from their liquid phase precursors. *Int. J. Mass Spectrom.* **2000,** *201*, 307-320.
25. Hoppilliard, Y.; Rogalewicz, F.; Ohanessian, G. Structures and fragmentations of zinc(II) complexes of amino acids in the gas phase. II. Decompositions of glycine–Zn(II) complexes. *Int. J. Mass Spectrom.* **2001,** *204*, 267-280.
26. Rogalewicz, F.; Hoppilliard, Y.; Ohanessian, G. Structures and fragmentations of zinc(II) complexes of amino acids in the gas phase. III. Rearrangement versus desolvation in the electrospray formation of the glycine-zinc complex. *Int. J. Mass Spectrom.* **2001,** *206*, 45-52.
27. Rogalewicz, F.; Hoppilliard, Y.; Ohanessian, G. Structures and fragmentations of zinc(II) complexes of amino acids in the gas phase: IV. Solvent effect on the structure of electrosprayed ions. *Int. J. Mass Spectrom.* **2003,** *227*, 439-451.
28. Frisch, M. J.; Trucks, G. W.; Schlegel, H. B.; Scuseria, G. E.; Robb, M. A.; Cheeseman, J. R.; Scalmani, G.; Barone, V.; Mennucci, B.; Petersson, G. A., et al. *Gaussian 09, Revision D.01* Gaussian, Inc.: Wallingford, CT, USA, 2009.
29. Weigend, F.; Ahlrichs, R. Balanced Basis Sets of Split Valence, Triple Zeta Valence and Quadruple Zeta Valence Quality for H to Rn: Design and Assessment of Accuracy. *Phys. Chem. Chem. Phys.* **2005,** *7*, 3297-3305.
30. Andrae, D.; Haeussermann, U.; Dolg, M.; Stoll, H.; Preuss, H. Energy-adjusted Ab Initio Pseudopotentials for the Second and Third Row Transition Elements. *Theor. Chim. Acta* **1990,** *77*, 123-141.
31. Feller, D. The Role of Databases in Support of Computational Chemistry Calculations. *J. Comput. Chem.* **1996,** *17*, 1571-1586.

32. Grimme, S.; Ehrlich, S.; Goerigk, L. Effect of the Damping Function in Dispersion Corrected Density Functional Theory. *J. Comput. Chem.* **2011,** *32*, 1456-1465.
33. Grimme, S.; Antony, J.; Ehrlich, S.; Krieg, H. A Consistent and Accurate Ab Initio Parametrization of Density Functional Dispersion Correction (DFT-D) for the 94 Elements H-Pu. *J. Chem. Phys.* **2010,** *132*, 154104-154119.
34. Polfer, N. C. Infrared Multiple Photon Dissociation Spectroscopy of Trapped Ions. *Chem. Soc. Rev.* **2011,** *40*, 2211−2221.
35. Kesharwani, M. K.; Brauer, B.; Martin, J. M. L. Frequency and Zero-Point Vibrational Energy Scale Factors for Double-Hybrid Density Functionals (and Other Selected Methods): Can Anharmonic Force Fields Be Avoided? *J. Phys. Chem. A* **2014,** *119*, 1701-1714.
36. Berglund, M.; Wieser, M. E. Isotopic Compositions of the Elements 2009 (IUPAC Technical Report). *Pure Appl. Chem.* **2011,** *83*, 397-410.
37. Shannon, R. D. Revised Effective Ionic Radii and Systematic Studies of Interatomic Distances in Halides and Chalcogenides. *Acta Cryst.* **1976,** *A32*, 751-767.
38. Foster, J. P.; Weinhold, F. Natural Hybrid Orbitals. *J. Am. Chem. Soc.* **1980,** *102*, 7211-7218.
39. Glendening, E. D.; Reed, A. E.; Carpenter, J. E.; Weinhold., F. *NBO Version 3.1*.
40. Corzana, F.; Busto, J. H.; Jiménez-Osés, G.; García de Luis, M.; Asensio, J. L.; Jiménez-Barbero, J.; Peregrina, J. M.; Avenoza, A. Serine versus Threonine Glycosylation: The Methyl Group Causes a Drastic Alteration on the Carbohydrate Orientation and on the Surrounding Water Shell. *J. Am. Chem. Soc.* **2007,** *129*, 9458-9467.
41. Madariaga, D.; Martínez-Sáez, N.; Somovilla, V. J.; García-García, L.; Berbis, M. Á.; Valero-Gónzalez, J.; Martín-Santamaría, S.; Hurtado-Guerrero, R.; Asensio, J. L.; Jiménez-Barbero, J., et al. Serine versus Threonine Glycosylation with α-O-GalNAc: Unexpected Selectivity in Their Molecular Recognition with Lectins. *Chem. Eur. J.* **2014,** *20*, 12616-12627.
42. Kisselev, A. F.; Songyang, Z.; Goldberg, A. L. Why Does Threonine, and Not Serine, Function as the Active Site Nucleophile in Proteasomes? *J. Biol. Chem.* **2000,** *275*, 14831-14837.

Table 1. Relative Energies (0 K) and Gibbs Energies (298 K) in kJ/mol of $Zn(Thr\text{-}H)^+(ACN)$ Complexes and its isomers[a]

structure	B3LYP/**GD3BJ**[b]	B3P86	MP2(full)
$[N,CO^-,OH_s]$-ggt(ACN)	0.8 (0.0) / **0.0 (0.0)**	2.9 (0.8)	0.0 (0.0)
$[N,O_s^-,CO]$-tgg(ACN)	0.0 (1.3) / **1.1 (2.0)**	0.0 (0.0)	1.5 (3.6)
$[N,O_s^-,CO]$-cgg(ACN)	19.1 (19.5) / **19.9 (13.9)**	18.7 (17.7)	21.2 (22.4)
$[N,O_s^-]$-tg_t(ACN)	31.2 (28.9) / **36.7 (27.6)**	36.9 (33.2)	41.8 (40.3)
$[N,CO^-]$-gtt(ACN)	33.3 (30.5) / **37.2 (29.1)**	38.8 (34.6)	42.2 (40.2)
$[N,O_s^-,OH]$-tgg(ACN)	36.8 (36.6) / **36.1 (37.9)**	40.2 (38.8)	35.6 (36.2)
$[N,CO^-]$-ttt(ACN)	39.5 (35.5)	45.5 (40.2)	48.8 (45.7)
$[N,O_s^-]$-tg+t(ACN)	43.2 (40.8)	50.1 (46.3)	52.1 (50.4)
$[CO^-,O_s^-](NH_3^+)$-cg(ACN)	46.4 (45.2)	50.6 (48.1)	53.7 (53.3)
$[N^-,CO,OH_s]$-tggt(ACN)	50.8 (45.9)	52.8 (46.6)	50.6 (46.6)
$[N,CO^-]$-tgg(ACN)	53.2 (51.1)	57.8 (54.4)	63.4 (62.1)
$[N,O_s^-]$-cgt(ACN)	56.9 (54.4)	61.6 (57.8)	67.0 (65.3)
$[N,O_s^-]$-ccg(ACN)	65.0 (69.6)	66.8 (70.1)	67.1 (72.6)
$[CO_2^-]$-ggt(ACN)	66.9 (61.0)	75.6 (68.4)	84.2 (79.1)
$[N,C_\gamma^-]$-tg_g_t(ACN)	67.0 (63.2)	68.4 (63.3)	67.7 (64.8)
$[CO^-,OH_s]$-cgc(ACN)	67.3 (64.9)	73.2 (69.5)	75.8 (74.2)
$[N^-,CO]$-tgtt(ACN)	69.1 (66.1)	74.7 (70.4)	80.5 (78.3)
$[N,C_\gamma^-]$-tg+g+t(ACN)	76.8 (71.4)	79.2 (72.4)	78.3 (73.7)
$[CO_2^-]$-gtt(ACN)	79.5 (71.2)	89.5 (79.9)	98.2 (90.7)
$[CO_2^-,OH_s]$-gcg(ACN)	81.0 (80.8)	82.6 (81.2)	85.2 (85.8)
$[N^-,OH_s]$-tttt(ACN)	84.0 (79.5)	92.4 (86.6)	90.6 (86.9)
$[N^-,OH_s]$-tgtt(ACN)	87.4 (80.5)	95.0 (86.8)	94.7 (88.7)
$[N^-,OH_s,OH]$-tggt(ACN)	87.8 (91.9)	93.2 (96.0)	85.5 (90.4)
$[O_s^-,OH]$-tgg(ACN)	104.7 (101.6)	115.6 (111.2)	113.5 (111.3)
$[N^-,OH]$-tgtt(ACN)	119.3 (114.9)	128.4 (122.7)	125.7 (122.1)
$Zn(Gly\text{-}H)^+(CH_3CHO)$(ACN)	-33.9 (-46.5)/**-24.8 (-40.6)**	-9.3 (-23.1)	5.9 (-5.8)

$Zn(Gly)^+(CH_3CO)(ACN)$	18.7 (6.2) / **29.5 (13.9)**	40.2 (26.3)	65.4 (53.6)
$ZnH(C_3H_7ON)^+(CO_2)(ACN)$	69.4 (50.1)	114.4 (93.8)	123.0 (104.4)
$ZnH(Gly\text{-}2H)^+(CH_3CHO)(ACN)$	87.8 (68.6)	132.9 (112.3)	152.5 (134.0)

[a] Relative single point energies in kJ/mol at 0 K and (in parentheses) 298 K Gibbs energies calculated at the level of theory indicated using a 6-311+G(2d,2p) basis set. [b] Empirical dispersion corrected B3LYP-GD3BJ values are given in bold.

Table 2. Relative Energies (0 K) and Gibbs Energies (298 K) in kJ/mol of $Zn(Gly\text{-}H)(ACN)^+$ Complexes[a]

structure	B3LYP/**GD3BJ**[b]	B3P86	MP2(full)
$Zn(Gly\text{-}H)^+[N,CO^-]$-c(ACN)	0.0 (0.0) / **0.0 (0.0)**	0.0 (0.0)	0.0 (0.0)
$Zn(Gly\text{-}H)^+[N^-,CO]$-tt(ACN)	7.1 (7.8) / **13.0 (10.6)**	5.4 (6.0)	8.3 (9.0)
$Zn(Gly\text{-}H)^+[CO_2^-]$-c(ACN)	19.0 (17.6) / **27.2 (14.2)**	20.6 (19.2)	28.1 (26.7)
$Zn(Gly\text{-}H)^+[N^-,CO]$-ct(ACN)	20.3 (28.0) / **22.5 (20.2)**	18.2 (25.8)	21.3 (29.0)
$Zn(Gly\text{-}H)^+[CO_2^-]$-c,$_{NH\cdot CO}$(ACN)	20.3 (24.9)	22.1 (26.6)	27.9 (32.4)
$Zn(Gly\text{-}H)^+[N,CO](C_\alpha^-)$-tt(ACN)	48.4 (51.2)	44.8 (47.5)	52.5 (55.2)
$Zn(Gly\text{-}H)^+[N,CO](C_\alpha^-)$-ct(ACN)	58.9 (61.1)	55.0 (57.2)	62.8 (65.0)
$Zn(Gly\text{-}H)^+[N^-,OH]$-tc(ACN)	65.2 (65.6)	67.1 (67.5)	61.6 (62.0)
$Zn(Gly\text{-}H)^+[C_\alpha^-,CO]$-cc(ACN)	87.5 (87.7)	85.3 (85.4)	99.0 (99.1)
$Zn(Gly\text{-}H)^+[C_\alpha^-,CO]$-tc(ACN)	92.7 (91.1)	93.7 (92.1)	105.9 (104.3)

[a] Relative single point energies (in kJ/mol) at 0 K and (in parentheses) 298 K Gibbs energies calculated at the level of theory indicated using a 6-311+G(2d,2p) basis set. [b] Empirical dispersion corrected B3LYP-GD3BJ values are given in bold.

Table 3. Relative Energies (0 K) and Gibbs Energies (298 K) in kJ/mol of $CdCl^+$(Thr) Complexes[a]

structure	B3LYP/**GD3BJ**[b]	B3P86	MP2(full)
[N,CO,OH_s]-tggt	0.0 (0.0) / **0.0 (0.0)**	0.0 (0.0)	0.0 (0.0)
[N,CO]-tg_g_+t	16.6 (14.9) / **23.2 (20.9)**	18.3 (16.6)	28.1 (26.4)
[CO_2^-]-ctgt	17.7 (14.4) / **30.6 (27.2)**	20.8 (17.4)	31.7 (28.4)
[CO_2^-]-cgtt	19.1 (14.8) / **31.9 (27.4)**	22.6 (18.4)	34.1 (29.9)
[N,CO]-tgtt	22.4 (19.6)	23.9 (21.1)	32.5 (29.7)
[N,CO]-tgtg	23.4 (20.3)	24.6 (21.5)	34.8 (31.7)
[N,CO,OH_s]-cggt	28.3 (28.0)	28.0 (27.7)	29.9 (29.6)
[N,OH_s]-tg_tt	28.8 (26.2)	31.7 (29.1)	35.3 (32.7)
[N,OH_s,OH]-tggt	29.8 (29.1)	32.0 (31.4)	26.6 (26.0)
[N,CO]-ccgt	31.5 (31.1)	30.7 (30.3)	45.5 (45.1)
[N,OH_s]-tg$_+$tt	38.7 (34.7)	42.7 (38.6)	45.3 (41.2)
[N,CO]-tg$_+$g_t	44.6 (41.6)	45.8 (42.8)	53.1 (50.1)
[CO,OH_s]-cggt	45.3 (43.5)	47.1 (45.4)	60.4 (58.6)
[N,CO]-tggg	45.9 (43.4)	47.1 (44.5)	55.5 (52.9)
[N,CO]-cgtt	47.3 (44.9)	48.1 (45.8)	57.8 (55.4)
[CO_2^-]-cggg	51.4 (46.6)	54.6 (49.8)	66.3 (61.5)
[CO_2^-]-cggt	54.5 (47.4)	58.2 (51.1)	69.9 (62.8)
[N,OH]-tgtt	58.7 (55.1)	62.4 (58.9)	62.8 (59.2)

[a] Relative single point energies (in kJ/mol) at 0 K and (in parentheses) 298 K Gibbs energies calculated at the level of theory indicated using a def2-TZVPP basis set and SDD ECP for Cd. [b]Empirical dispersion corrected B3LYP-GD3BJ values are given in bold.

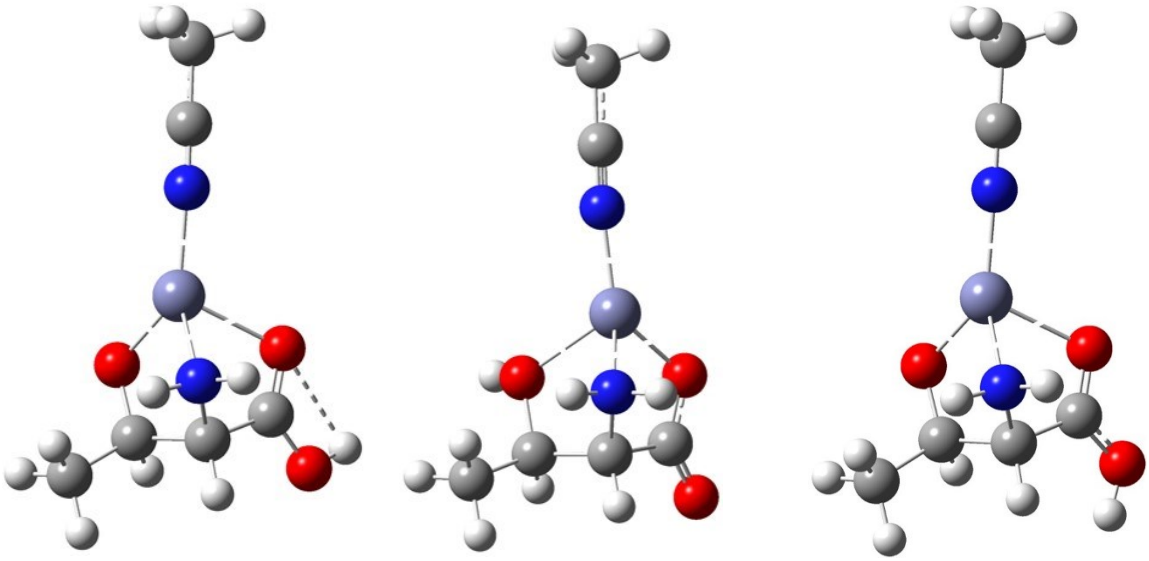

[N,O_s^-,CO]-tgg(ACN) [N,CO^-,OH_s]-ggt(ACN) [N,O_s^-,CO]-cgg(ACN)

(1.3, 2.0, 0.0, 3.6) (0.0, 0.0, 0.8, 0.0) (19.5, 13.9, 17.7, 22.4)

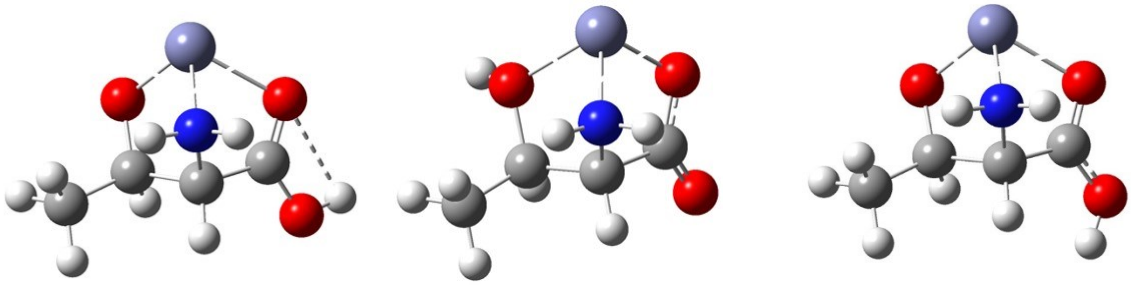

[N,O_s^-,CO]-tgg [N,CO^-,OH_s]-ggt [N,O_s^-,CO]-cgg

(0.0, 0.0, 0.0, 0.0) (11.8, 9.9, 14.6, 8.8) (21.5, 21.0, 21.0, 21.7)

Figure 1. Structures of the lowest-energy located $Zn(Thr\text{-}H)^+(ACN)$ and $Zn(Thr\text{-}H)^+$ conformers calculated at the B3LYP/6-311+G(d,p) level of theory. Relative 298 K Gibbs energies in kJ/mol are given at the B3LYP, B3LYP-GD3BJ, B3P86, and MP2(full) levels, respectively. Short dashed lines indicate hydrogen bonds. Metal-ligand interactions are shown by long dashed lines. (Red—oxygen, grey—carbon, white—hydrogen, blue—nitrogen, steel grey—zinc.)

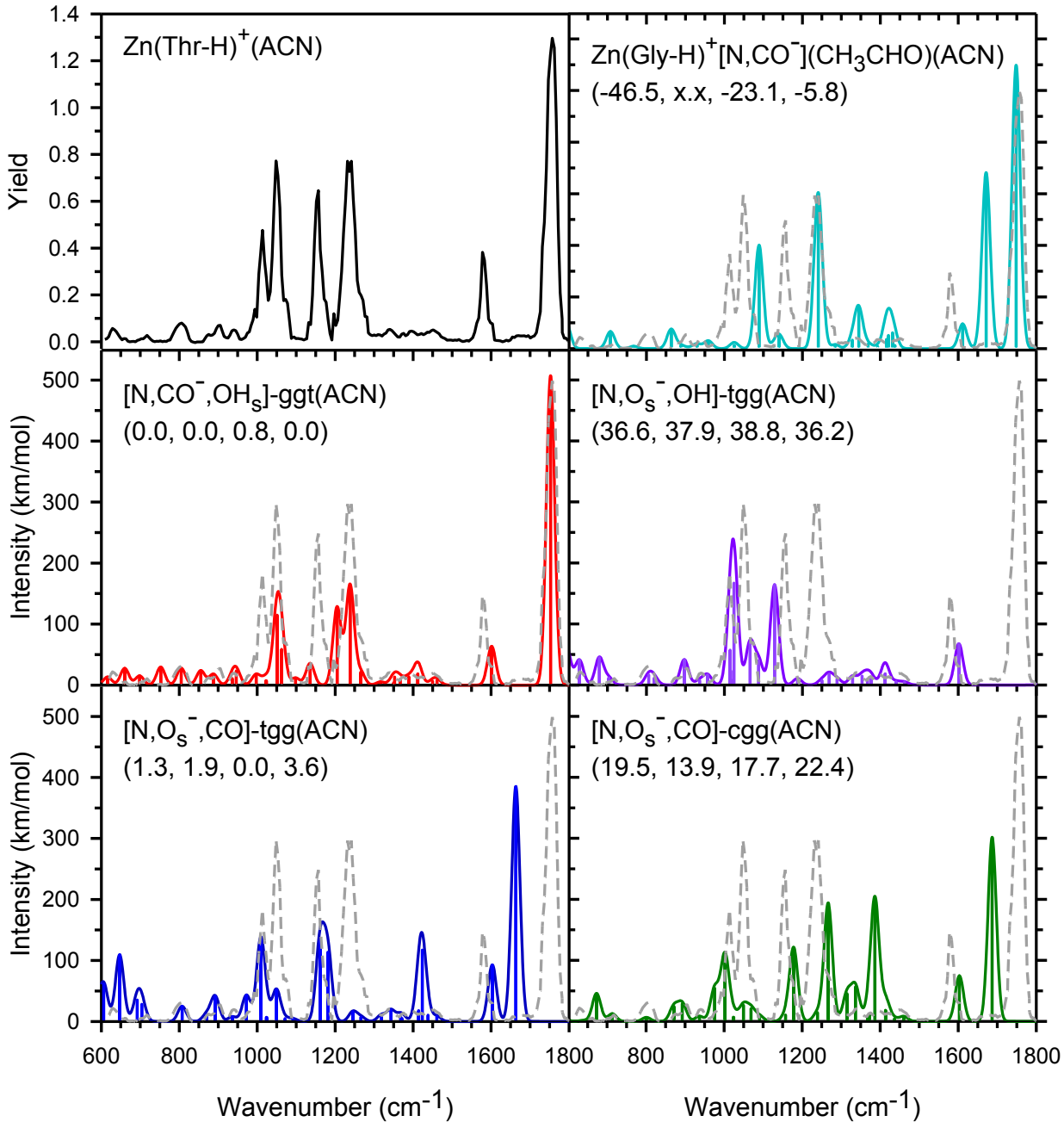

Figure 2. Comparison of the Zn(Thr-H)$^+$(ACN) experimental IRMPD action spectrum with IR spectra calculated at the B3LYP/6-311+G(d,p) level of theory for low-lying conformers. Relative 298 K Gibbs energies in kJ/mol are given at the B3LYP, B3LYP-GD3BJ, B3P86, and MP2(full) levels, respectively.

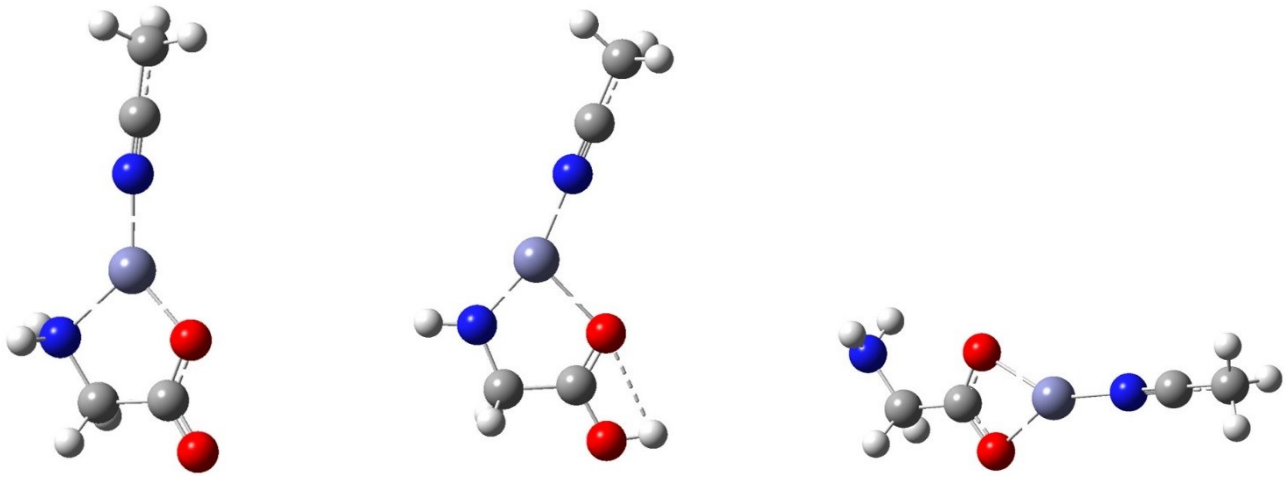

$Zn(Gly\text{-}H)^+[N,CO^-]$-c(ACN)	$Zn(Gly\text{-}H)^+[N^-,CO]$-tt(ACN)	$Zn(Gly\text{-}H)^+[CO_2^-]$-c(ACN)
(0.0, 0.0, 0.0, 0.0)	(7.8, 10.6, 6.0, 9.0)	(17.6, 14.2, 19.2, 26.7)

Figure 3. Structures of $Zn(Gly\text{-}H)^+$ conformers calculated at the B3LYP/6-311+G(d,p) level of theory. Relative 298 K Gibbs energies in kJ/mol are given at the B3LYP, B3LYP-GD3BJ, B3P86, and MP2(full) levels, respectively. Short dashed lines indicate hydrogen bonds. Metal-ligand interactions are shown by long dashed lines. (Red—oxygen, grey—carbon, white—hydrogen, blue—nitrogen, steel grey—zinc.)

Figure 4. Comparison of the $Zn(Gly\text{-}H)^+(ACN)$ experimental IRMPD action spectrum with IR spectra calculated at the B3LYP/6-311+G(d,p) level of theory for low-lying conformers. Relative 298 K Gibbs energies in kJ/mol are given at the B3LYP, B3LYP-GD3BJ, B3P86, and MP2(full) levels, respectively.

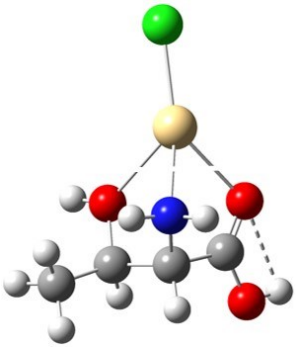

$[N,CO,OH_s]$-tggt

(0.0, 0.0, 0.0, 0.0)

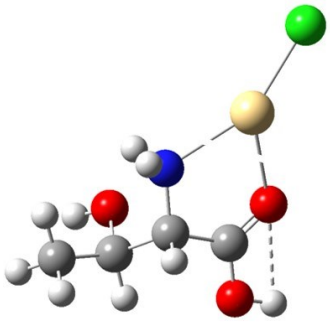

$[N,CO]$-tg_g+t

(14.9, 20.9, 16.6, 26.4)

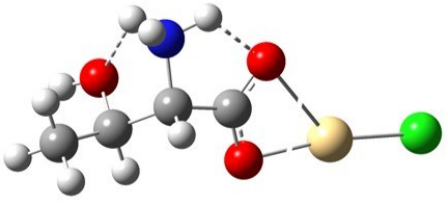

$[CO_2^-]$-ctgt

(14.4, 27.2, 17.4, 28.4)

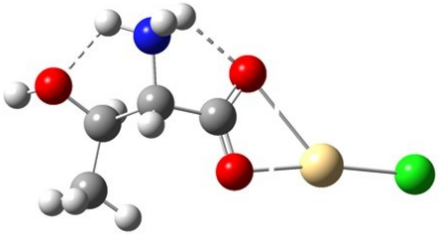

$[CO_2^-]$-cgtt

(14.8, 27.4, 18.4, 29.9)

Figure 5. Structures of select $CdCl^+(Thr)$ conformers calculated at the B3LYP/def2-TZVP level of theory. Relative 298 K Gibbs energies in kJ/mol are given at the B3LYP, B3LYP-GD3BJ, B3P86, and MP2(full) levels, respectively. Short dashed lines indicate hydrogen bonds. Metal-

ligand interactions are shown by long dashed lines. (Red—oxygen, grey—carbon, white—hydrogen, blue—nitrogen, yellow—cadmium, green—chlorine.)

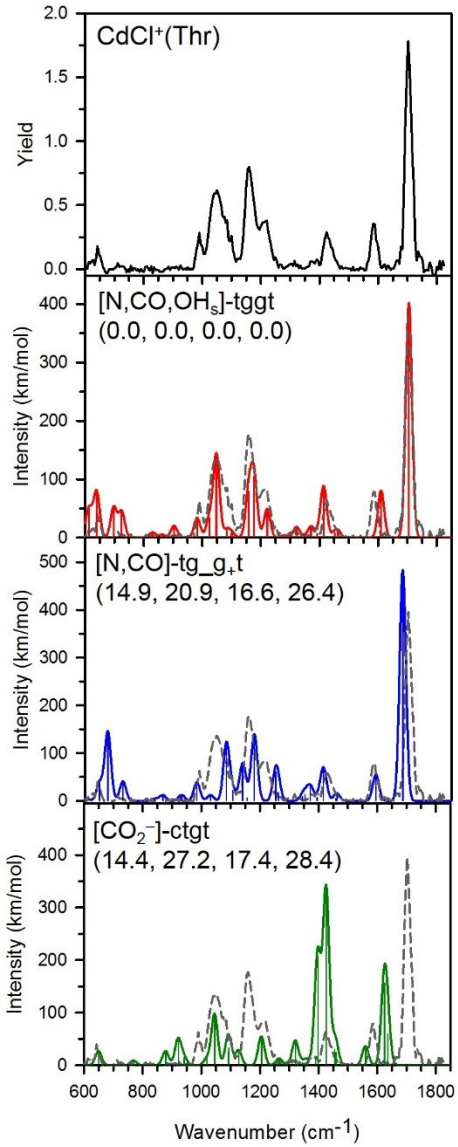

Figure 6. Comparison of the $CdCl^+$(Thr) experimental IRMPD action spectrum with IR spectra calculated at the B3LYP/def2-TZVP level of theory for low-lying conformers. Relative 298 K Gibbs energies in kJ/mol are given at the B3LYP, B3LYP-GD3BJ, B3P86, and MP2(full) levels, respectively.